SPECIAL
International Precipitation Working Group
COLLECTION

Intercomparison of Rainfall Estimates from Radar, Satellite, Gauge, and Combinations for a Season of Record Rainfall

JONATHAN J. GOURLEY

NOAA/National Severe Storms Laboratory, Norman, Oklahoma

YANG HONG

Department of Civil Engineering and Environmental Science, University of Oklahoma, Norman, Oklahoma

ZACHARY L. FLAMIG

NOAA/National Severe Storms Laboratory, and Cooperative Institute for Mesoscale Meteorological Studies, University of Oklahoma, Norman, Oklahoma

LI LI AND JIAHU WANG

Department of Civil Engineering and Environmental Science, University of Oklahoma, Norman, Oklahoma

(Manuscript received 1 June 2009, in final form 16 September 2009)

ABSTRACT

Rainfall products from radar, satellite, rain gauges, and combinations have been evaluated for a season of record rainfall in a heavily instrumented study domain in Oklahoma. Algorithm performance is evaluated in terms of spatial scale, temporal scale, and rainfall intensity. Results from this study will help users of rainfall products to understand their errors. Moreover, it is intended that developers of rainfall algorithms will use the results presented herein to optimize the contribution from available sensors to yield the most skillful multisensor rainfall products.

1. Introduction

Accurate rainfall measurement is needed for a variety of applications vital to the economy, natural resources, and social infrastructure including agriculture, flash flood detection and prediction, water resources management, drinking water supplies, dam operations, transportation, hydroelectric power generation, water quality modeling, debris flow prediction, etc. However, accurately measuring rainfall has been a challenge to the research community predominantly because of its high variability in space and time. A rain gauge, for instance, collects rainfall directly in a small orifice and measures the water depth, weight, or volume. While the point measurement is considered accurate with quantifiable errors, the sampled rainfall rate often does not represent rainfall in close proximity, which becomes particularly problematic for intense rainfall with high spatial variability (Zawadzki 1975).

Remote sensing platforms, such as radar and satellite, provide an indirect measure of rainfall using passive or active radiation sensors. These sensors have been shown to reveal spatial patterns of rainfall at scales unachievable with operational rain gauge networks, and they provide measurements over sparsely populated and oceanic regions that have been previously unobserved. The indirectness of distant radiance measurements to surface rainfall rate, however, introduces a host of uncertainties, many of which are difficult to quantify. [The reader is referred to Zawadzki (1975), Marselek (1981), Legates and DeLiberty (1993), Nystuen (1999), and Ciach (2003) for a summary of quantitative precipitation estimation (QPE) errors when compared with gauges]. Relevant literature reviews of radar-based rainfall errors can be found in Wilson and Brandes (1979), Austin (1987), and

Corresponding author address: Jonathan J. Gourley, National Weather Center, 120 David L. Boren Blvd., Norman, OK 73072-7303.
E-mail: jj.gourley@noaa.gov

DOI: 10.1175/2009JAMC2302.1

Joss and Waldvogel (1990). Recent articles discussing errors in high-resolution satellite precipitation products can be found in Steiner et al. (2003), Anagnostou (2004), Gebremichael and Krajewski (2004), Hong et al. (2006), Ebert et al. (2007), Hossain and Huffman (2008), and others.

Recent developments in QPE have taken a more holistic approach of utilizing the various strengths of the available in situ and remotely sensed measurements to yield a multisensor estimate of rainfall (e.g., Gourley et al. 2002; Vasiloff et al. 2007). The primary objective of this study is to identify the strengths and weaknesses of operational and research rainfall products as a function of space, time, and rainfall intensity over a study region where there is excellent radar coverage and a dense gauge network. We provide an analysis of the spatial patterns, temporal variability, and intensities of rainfall from satellites, radars, rain gauges, and combinations. The secondary objective of this study is to help guide users of the individual algorithms, so that the rainfall products can be appropriately utilized for various applications in other regions outside of Oklahoma where sensor coverage is sparse, such as in the intermountain west of the United States (Maddox et al. 2002) and many developing countries. The reader is reminded that the study region is relatively flat and the rainfall is from intense, convection storms; variations in algorithm performance from the results reported herein may occur because of regional topographic and climatological rainfall differences. *One ultimate but far-reaching goal is to provide quantitative information regarding algorithm skill as a function of spatial scale, temporal scale, and rainfall intensity so that QPE algorithm developers can optimize their contribution in a multisensor framework.*

The paper is organized as follows: Section 2 describes the study region, observing platforms, and suite of rainfall algorithms evaluated for a summer season of record rainfall in 2007. Section 3 provides an analysis of the spatial characteristics and error quantification for seasonal rainfall accumulations. Daily accumulations are first evaluated in a bulk sense, then as a function of rainfall intensity using contingency table statistics. The ability of the algorithms to represent the diurnal cycle and hourly rainfall patterns is assessed. A summary of results and conclusions are provided in section 4.

2. Study domain and rainfall algorithms

a. Study area

The analysis focuses on rainfall from June to August 2007 over the state of Oklahoma. The Oklahoma Climate Survey reported June 2007 as the wettest month on record since 1895 for four out of nine climate divisions in the state. For the state overall, this was the wettest month on record. The recurrence of daily rainfall in Oklahoma City, Oklahoma, was also a record with 20 days of consecutive rainfall from 13 June to 2 July. The previous record was 14 consecutive days of reported rainfall set in the spring of 1937. The state had 15 days of damaging flash floods, with the biggest contribution from a strengthening Tropical Storm Erin impacting the region from 17 to 20 August 2007 (Arndt et al. 2009). The Fort Cobb mesonet station recorded 187 mm of rainfall in 3 h, which was considered a 500-yr event. The intensity of extreme rainfall provides a unique dataset to study. This data archive also invites future investigations of local and regional hydrologic impacts.

The study domain, extending from 34.0° to 37.0° latitude and from −100.0° to −95.0° longitude, is shown in gray in Fig. 1. The blue dots show 944 gauge locations in the study region composing the Hydrometeorological Automated Data System (HADS) network operated by the Office of Hydrologic Development of the U.S. National Weather Service (NWS). The red triangles show four Weather Surveillance Radar-1988 Doppler (WSR-88D) that are part of the operational Next Generation Weather Radar (NEXRAD) network. Data from the gauges and radars shown in Fig. 1 are used to build the gauge-based, radar-based, and blended radar–gauge–human rainfall products described below.

b. Ground rainfall products

The gauge-based product used here is the 4-km U.S. gridded gage-only hourly precipitation analysis developed for operational use by the National Centers for Environmental Prediction (NCEP) Environmental Modeling Center (EMC; available online at http://data.eol.ucar.edu/codiac/dss/id=21.088). The product is derived from automated rain gauge reports from several networks with different reporting intervals, maintenance requirements, gauge types, wind screening, and quality control procedures applied. Because the gauges are automated, most of the instruments are either tipping bucket or weighing gauges. Erroneous rain gauge data are removed according to a manually edited, infrequently updated ''bad gauge list.'' Rain gauge measurements are objectively analyzed on a grid having 4.76-km spacing using the optimal estimation technique described in Seo (1998). The method accounts for the fractional coverage of rainfall due to sparse gauge networks and rainfall fields with high spatial variability. A benefit is accurate delineation of rain versus no-rain regions. This study refers to the NCEP Stage II gauge-based product simply as ''Gauge'' with hourly accumulations available on a 4.76-km grid at the top of each hour.

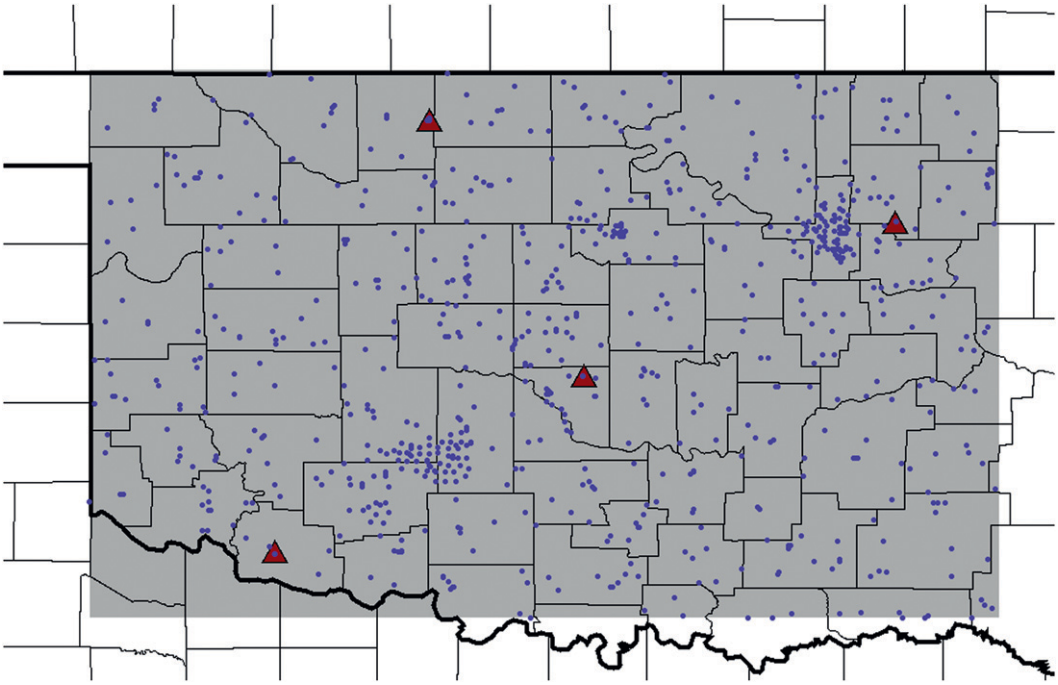

FIG. 1. Study region (shaded in gray) showing 944 rain gauges (filled circles in blue) composing the Hydrometeorological Automated Data System and four WSR-88D (red triangles).

The radar-based product, formally referred to as the 4-km NCEP/EMC U.S. gridded radar-estimated precipitation with no bias removal, was generated operationally, archived, and then retrieved online (http://data.eol.ucar.edu/codiac/dss/id=21.090). The radar-only product has also been referred to in other studies as the Stage II radar-only or RAD product; in this study, it is referred to hereinafter as ''Radar.'' Rainfall estimates are produced from data collected on a hybrid of radar elevation angles constructed to maximize low-level coverage at each WSR-88D site using a reflectivity–rainfall (Z–R) relation. No quality control measures are taken at this stage of operational processing to correct for nonweather scatterers such as biological targets or anomalous propagation. The rainfall estimates from adjacent radars are then merged onto the same 4.76-km grid as the Gauge using an inverse distance-weighting scheme.

The NCEP hourly multisensor precipitation analysis, or Stage IV hereinafter, combines rainfall estimates from WSR-88D radar, rain gauges, and satellite, with quality control performed manually by NWS forecasters. The NCEP Stage IV product is a mosaic of multisensor rainfall products produced by the individual River Forecast Centers (RFCs). Additional details of the algorithm can be found online (see http://www.emc.ncep.noaa.gov/mmb/ylin/pcpanl/stage4/). The technique of merging radar and rain gauge estimates has its roots in the precipitation processing algorithm 1 (P1) method originally developed at the Arkansas–Red Basin RFC. A spatially variable bias field is computed by comparing radar-estimated rainfall (i.e., the Radar described above) to rain gauge measurements each hour. The bias field is then analyzed on a 4.76-km grid using a weighted interpolation scheme. The bias is then applied to the radar field so that the spatial variability of rainfall resolved by radar is preserved, while the amounts are calibrated to collocated rain gauge amounts. There is the potential in the algorithm for the forecaster to use rainfall estimates from the Hydro-Estimator algorithm developed at the National Environmental Satellite, Data, and Information Service (Vicente et al. 1998; Scofield and Kuligowski 2003). However, satellite data are used in the study domain very rarely (B. Lawrence, Arkansas–Red Basin RFC, 2009, personal communication); thus the Stage IV product is built with radar rainfall estimates and rain gauge measurements, with careful quality control performed manually by operational forecasters.

c. *Satellite rainfall products*

In recent years, satellite-based precipitation estimates have been developed on subdaily time resolution over the globe by combining information from microwave (MW) and infrared (IR) observations (Hsu et al. 1997; Sorooshian et al. 2000; Kidd et al. 2003; Hong et al. 2004; Joyce et al. 2004; Turk and Miller 2005; Huffman et al. 2007). Two operational quasi-global satellite rainfall

products used in this study are the Tropical Rainfall Measuring Mission (TRMM) Multisatellite Precipitation Analysis (TMPA; Huffman et al. 2007) and Precipitation Estimation from Remotely Sensed Information using Artificial Neural Networks-Cloud Classification System (PERSIANN-CCS; Hong et al. 2004).

TMPA provides precipitation estimates by combining information from multiple satellites as well as rain gauges depending on sensor availability. The TRMM products are available 3-hourly at 0.25° × 0.25° spatial resolution covering the globe 50°S–N latitude. TMPA provides two standard 3B42-level products for the research community: the near-real-time 3B42RT and post-real-time 3B42V6. The real-time product, 3B42RT, uses the TRMM Combined Instrument (TCI; TRMM precipitation radar and TRMM Microwave Imager) dataset to calibrate precipitation estimates derived from available low-Earth-orbiting passive microwave radiometers and then merges all these estimates at 3-h intervals. Gaps in these analyses are filled using geosynchronous infrared data regionally calibrated to the merged microwave product. The post-real-time product, 3B42V6, adjusts the monthly accumulations of the 3-hourly fields from 3B42RT based on a monthly gauge analysis, including the Climate Assessment and Monitoring System (CAMS) 0.5° × 0.5° monthly gauge analysis and the Global Precipitation Climatology Center (GPCC) 1.0° × 1.0° monthly gauge product. The monthly ratio of the satellite-only and satellite–gauge combination is used to rescale the individual 3-h estimates. Therefore, the gauge-adjusted final product, 3B42V6, has a nominal resolution of 3-h time step (0000, 0300, . . . , 2100 UTC) and 0.25° × 0.25° spatial resolution, within the global latitude belt 50°S–50°N. More recently, Huffman et al. (2009) describe how the 3B42RT product is scaled using the TRMM Combined Instrument. Applying a bias correction without the need for monthly gauge accumulations will have significant benefits for real-time users of rainfall products, especially in ungauged basins.

PERSIANN-CCS has been evaluated in the continental United States for its general performance (Hong et al. 2004) and in the complex terrain region in western Mexico for its ability to capture the climatological structure of precipitation with respect to the diurnal cycle and regional terrain features (Hong et al. 2007). The PERSIANN-CCS algorithm extracts local and regional cloud features from infrared geostationary satellite imagery in estimating a finer-scale (i.e., 0.04° × 0.04°, 30 min) rainfall distribution. PERSIANN-CCS is able to generate various rain rates at a given brightness temperature (T_b) and variable rain/no-rain IR thresholds for different cloud types, which overcomes the one-to-one mapping limitation of a single T_b–rainfall rate (R) function for the full spectrum of cloud–rainfall conditions. There are also two versions of PERSIANN-CCS products available, a real-time (PERSIANN-CCS-RT) version and a microwave-adjusted (PERSIANN-CCS-MW) version. First, the PERSIANN-CCS-RT algorithm processes real-time Geostationary Operational Environmental Satellite (GOES) cloud images into pixel rain rates as described in Hong et al. (2004). Afterward, in the PERSIANN-CCS-MW algorithm, an automated neural network for cloud patch–based rainfall estimation, entitled the Self-Organizing Nonlinear Output (SONO) model (Hong et al. 2005), was developed to adjust the real-time product by using composite microwave precipitation estimates from low-Earth-orbiting satellite platforms, such as TRMM. The MW-based precipitation estimates are used to rescale the PERSIANN-CCS-RT rainfall products on a seasonal (3-monthly) basis. The real-time data from the current version of PERSIANN-CCS-RT are available online both at regional (http://hydis8.eng.uci.edu/CCS/) and global scales (http://hydis8.eng.uci.edu/GCCS/). However, the PERSIANN-CCS-MW product is processed and archived after several days of delay.

The radar, gauge, and Stage IV rainfall products were produced on an NWS Hydrologic Rainfall Analysis Project (HRAP) grid having 4.76-km resolution and a polar stereographic projection. Geographic information systems scripts were used to reproject and resample all NCEP rainfall products onto an analysis grid with a geographic, or latitude/longitude, projection having 0.04° × 0.04° resolution. The TRMM and PERSIANN-CCS satellite QPE products were also resampled onto the same 0.04°-resolution grid in geographic coordinates containing the radar, gauge, and Stage IV products. Because the native spatial resolution of the TRMM-3B42RT and TRMM-3B42V6 products is 0.25°, the analysis grid oversamples their values. No interpolation methods were used in the centroid-based resampling; values coincident with the centroid of each analysis grid point were used directly.

3. Results

a. Seasonal accumulations

Rainfall rates from all products have been accumulated from June to August 2007 to yield seasonal totals in Fig. 2. The TRMM-3B42RT and TRMM-3B42V6 products are noticeably coarser in resolution compared to the other products. The TRMM-3B42RT product identifies rainfall maxima in the central part of the domain. It also indicates a secondary rainfall maximum in the far southeast part. The TRMM-3B42V6 product has substantially lower accumulations than the TRMM-3B42RT

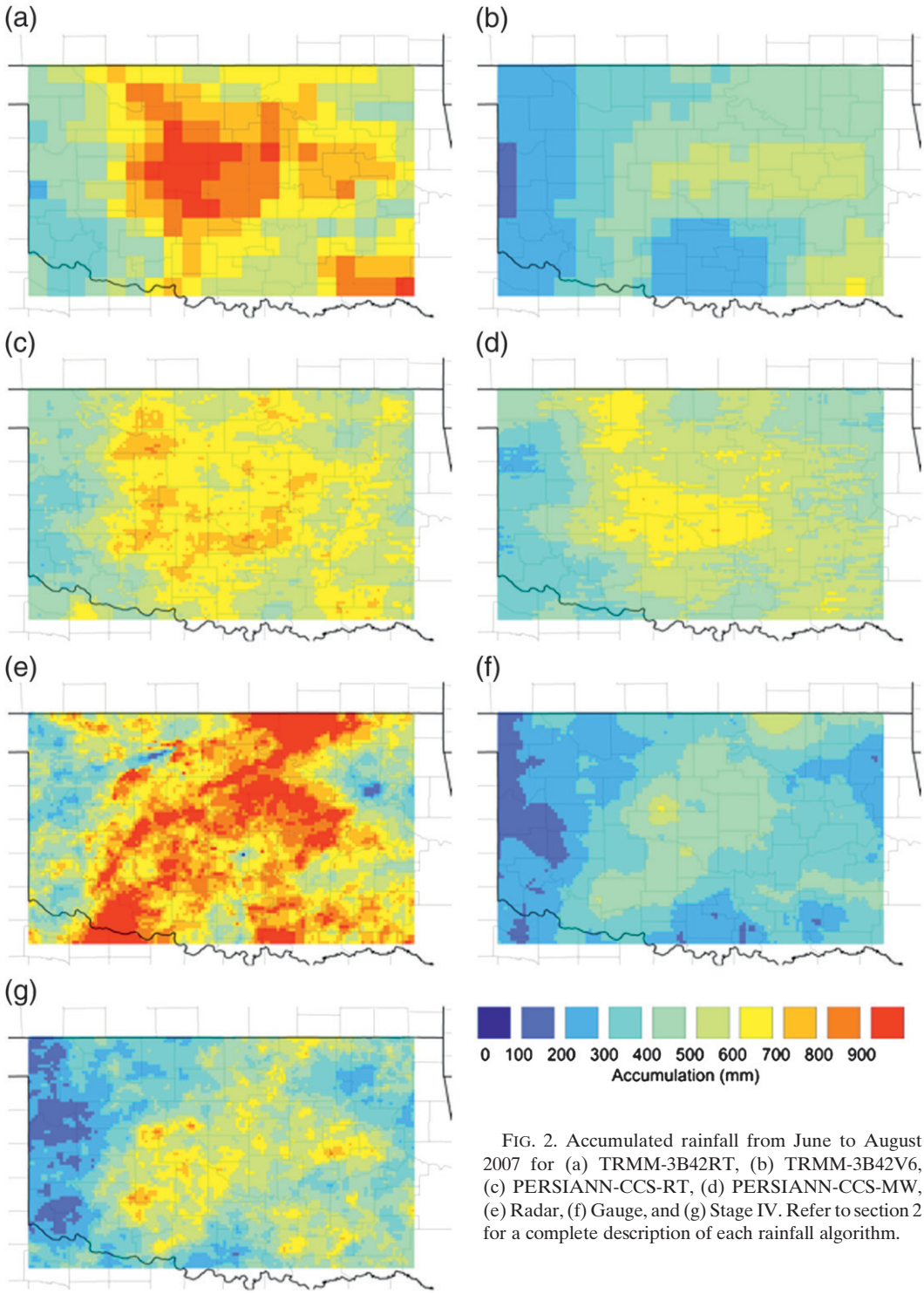

FIG. 2. Accumulated rainfall from June to August 2007 for (a) TRMM-3B42RT, (b) TRMM-3B42V6, (c) PERSIANN-CCS-RT, (d) PERSIANN-CCS-MW, (e) Radar, (f) Gauge, and (g) Stage IV. Refer to section 2 for a complete description of each rainfall algorithm.

product (Fig. 2b). It is also noted that the spatial pattern of the seasonal rainfall is different in comparing the two products. Rainfall in the northwestern part of the state has been reduced by as much as 500 mm in Fig. 2b, while the maxima in the eastern and southeastern part of the state were reduced by approximately 250 mm. The PERSIANN-CCS-RT and PERSIANN-CCS-MW products have precipitation maxima in the central and northern parts and minima in the far west. The rainfall patterns in Figs. 2c and 2d resemble each other and those shown

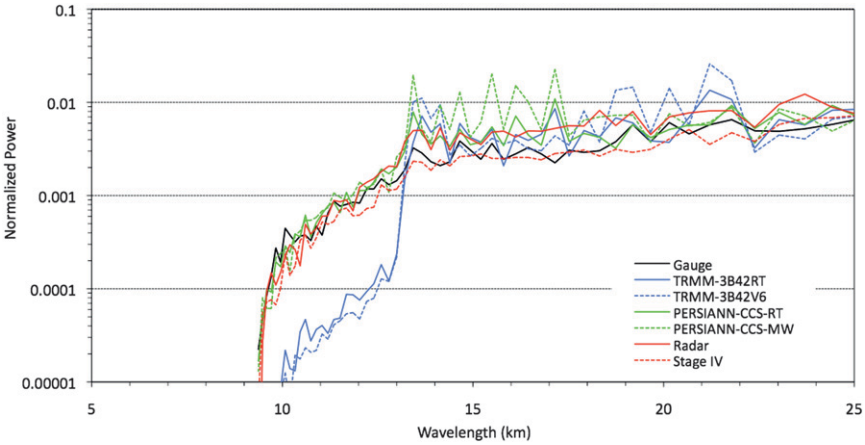

FIG. 3. Normalized power spectrum computed using a discrete Fourier transform for seasonal accumulations shown in Fig. 2.

in Fig. 2a. In comparing the two PERSIANN-CCS products, the rainfall amounts in Fig. 2d are lower by approximately 20% because of the adjustment using passive microwave rain rates. The Radar has the highest accumulations of all products while rainfall maxima are focused in a band extending from southwest to northeast, and a separate region in the southeast (Fig. 2e). Distinct minima are coincident with three of the radar sites. In the northwest, there is an apparent blockage to the southwest of the radar that creates a wedge of anomalously low accumulations. The Gauge in Fig. 2f has the lowest accumulations of all products and indicates a band of precipitation extending from the southwest to northeast and a separate region in the southeast, similar in shape to the Radar. The Gauge seasonal accumulation has a smooth appearance, similar to that in Fig. 2b, and reveals individual rainfall maxima having circular shapes that are most likely a result of the analysis scheme.

The Stage IV product in Fig. 2g does an admirable job of mitigating the artifacts noted in Figs. 2e and 2f, captures the spatial details captured by Radar, and effectively calibrates the Radar amounts to closer agreement with Gauge accumulations. The Stage IV product has also had manual quality control procedures applied as described in section 2. For these reasons, the Stage IV product will be used as a benchmark, or ground truth, in comparing the algorithms in forthcoming analyses. In comparing the TRMM and PERSIANN-CCS rainfall patterns with Stage IV, Figs. 2a, 2c, and 2d all yield erroneously high accumulations in the northwestern part of the domain. While the Radar, Gauge, and Stage IV analyses all imply a southwest–northeast orientation of the heaviest rainfall, the satellite products appear to suggest a more west–east orientation. All satellite products manage to capture the separate rainfall maximum in the southeast part of the State, however it is depicted too far to the south.

To quantify the spatial scales of rainfall resolved by each of the seasonal accumulations, we have transformed the data shown in Fig. 2 into the frequency domain using a discrete Fourier transform. Figure 3 shows the normalized power spectrum for each QPE algorithm. This analysis indicates that rainfall structures are poorly resolved by TRMM-3B42RT and TRMM-3B42V6 in comparison with the other products for wavelengths between 9 and 13 km. The lower bound of 9 km corresponds to the minimum wavelength needed to resolve the spatial scale of the true seasonal rainfall accumulation. This means a grid with a resolution of twice this wavelength, or 18 km, would have been sufficient to capture the inherent spatial rainfall variability. The TRMM-3B42RT and TRMM-3B42V6 products capture the spatial rainfall variability for wavelengths greater than 13 km; this wavelength corresponds to approximately one-half the resolution of the 0.25° × 0.25° grid spacing of the TRMM rainfall products.

A quantitative analysis of the rainfall products is provided by comparing the seasonal accumulations to the Stage IV product on a cell-by-cell basis, yielding a sample size of 123 columns by 74 rows in the analysis grid equaling 9102 points. The validity of the evaluation is conditional on the accuracy of the Stage IV product, and thus the reader is encouraged to view these analyses as relative and not necessarily absolute. The reader is also reminded that the Stage IV product is not independent from the Radar or Gauge; we expect to see similarities between these products because they use the same information. Scatterplots of Stage IV versus each of the evaluated QPE algorithms are shown on a log-log scale in Fig. 4. Each panel indicates the normalized bias (NB

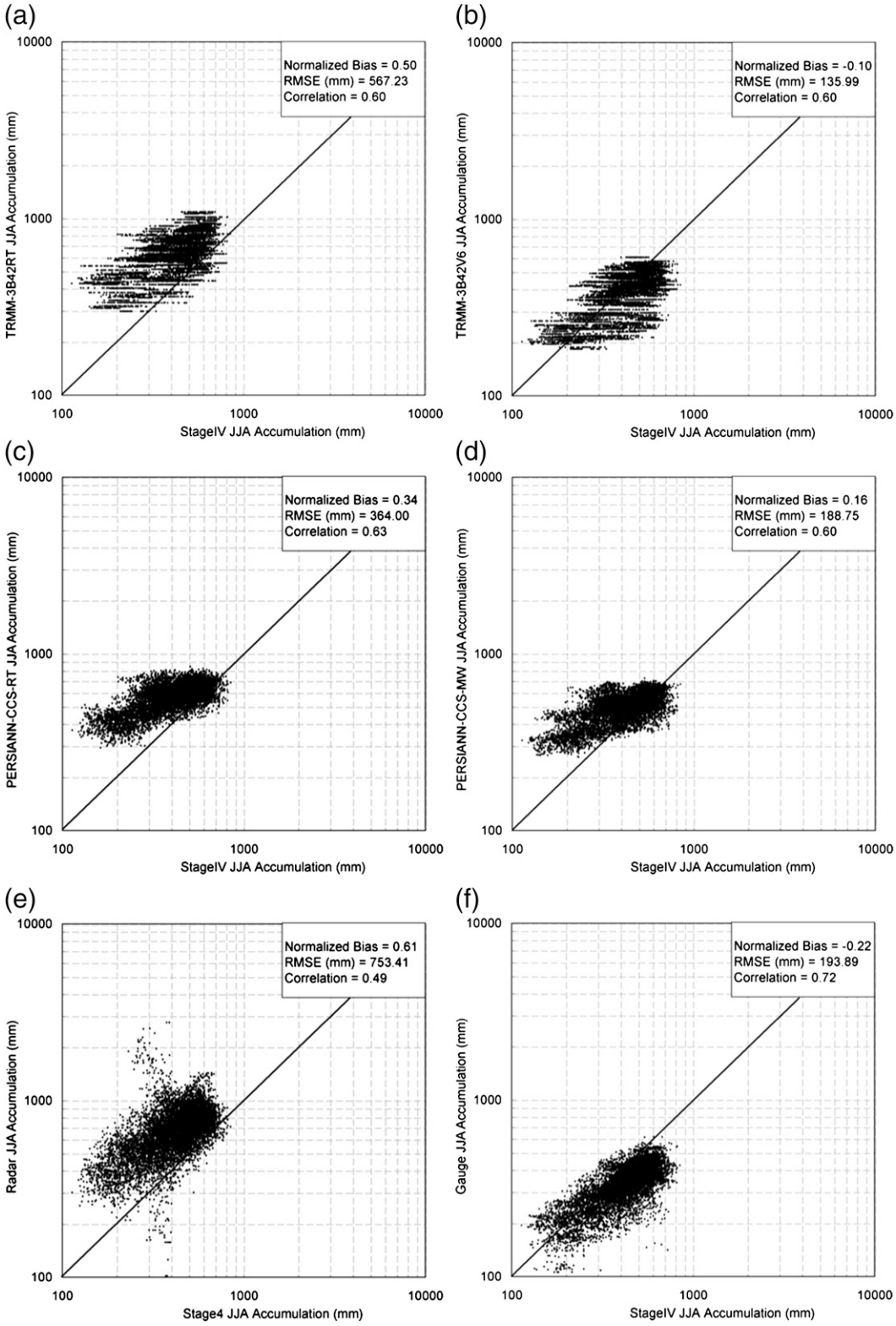

FIG. 4. Scatterplots that show seasonal rainfall accumulations shown in Fig. 2 in comparison with Stage IV rainfall. Bulk statistics summarizing their performance are shown in the upper-right corner of each panel.

hereinafter), root-mean-square error computed after the bias was removed (RMSE hereinafter), and Pearson correlation coefficient (CORR), defined as follows:

$$\mathrm{NB} = \frac{\sum \mathrm{QPE}_i - \mathrm{StageIV}_i}{\sum \mathrm{StageIV}_i}, \tag{1}$$

$$\mathrm{RMSE} = \left\langle \left(\mathrm{QPE} \times \frac{\sum \mathrm{StageIV}_i}{\sum \mathrm{QPE}_i} - \mathrm{StageIV} \right)^2 \right\rangle^{1/2}, \tag{2}$$

and

$$\mathrm{CORR} = \frac{\mathrm{cov}(\mathrm{QPE},\ \mathrm{StageIV})}{\sigma_{\mathrm{QPE}} \sigma_{\mathrm{StageIV}}}, \tag{3}$$

where NB is dimensionless, RMSE is in millimeters, and CORR is dimensionless. The angled brackets in (2) refer to averaging. In the computation of CORR, cov refers to the covariance, and σ is the standard deviation. NB, when multiplied by 100, gives the degree of overestimation or underestimation in percentage.

The real-time TRMM product, TRMM-3B42RT, overestimated rainfall by 50%, had an RMSE of 567 mm and a comparatively good CORR of 0.60 (Fig. 4a). The TRMM-3B42V6 product had the lowest NB of −0.10, indicating underestimation of 10% (Fig. 4b). This product also had the lowest RMSE (136 mm) when compared with the other algorithms. The PERSIANN-CCS-RT product performed better than TRMM-3B42RT according to all three statistics (Fig. 4c). The PERSIANN-CCS-MW product offered improvements over PERSIANN-CCS-RT in terms of cutting the NB and RMSE approximately in half but reduced the CORR from 0.63 to 0.60 (Fig. 4d). Overestimation with the Radar algorithm was 61%; this algorithm also had the largest scatter as represented with an RMSE of 753 mm and lowest CORR of 0.49 (Fig. 4e). The Gauge, on the other hand, underestimated rainfall by 22% (Fig. 4f). The Gauge had the highest CORR of all QPE algorithms at 0.72. In summary, the best overall performance in terms of seasonal NB and RMSE was with the TRMM-3B42V6 product despite its coarse resolution, while the worst overall performance was with Radar. It is noteworthy that both satellite algorithms that had no gauge adjustment (i.e., TRMM-3B42RT and PERSIANN-CCS-RT) outperformed the unadjusted Radar in terms of all three performance measures. At the seasonal time scale, it appears that satellite is superior to radar prior to the application of rain gauge adjustments.

b. Daily statistics

Daily accumulations were created for the PERSIANN-CCS-RT, PERSIANN-CCS-MW, Radar, Gauge, and Stage IV products by simply adding up 24 hourly accumulations for each day. The TRMM rainfall products are available on a nominal 3-hourly basis at 0000, 0300, 0600, 0900, 1200, 1500, 1800, and 2100 UTC as described in Huffman et al. (2007). The accumulations were centered on the nominal observation times at which the passive microwave fields were converted to precipitation estimates. Daily accumulations were created by summing the files from 0300 to 2100 UTC plus one-half the 0000 UTC accumulation of the same day and one-half the 0000 UTC accumulation for the next day. Once again, we assume the Stage IV product is the benchmark and compare daily accumulations from each of the algorithms on a cell-by-cell basis. The sample size is $123 \times 74 \times 92 = 837\ 384$ corresponding to the number of columns and rows composing the analysis grid and number of days in June–August.

The same bulk statistics used in the seasonal evaluation in section 3a are used here, but were computed on a daily basis and are thus shown as histograms of NB, RMSE, and CORR (Fig. 5). Figure 5a indicates Radar had the largest, or worst, NB with a mode in the 60% overestimation bin, while the Gauge product had the best NB with a mode in the 0% bin. The TRMM-3B42V6 reanalysis product improved over its real-time counterpart by shifting the distribution closer to the 0% bin. The distributions for PERSIANN-CCS-RT and PERSIANN-CCS-MW are similar with the latter product offering some improvement at the tails of the distribution and increasing the frequency of points falling in the 0% bin. The histograms of daily RMSE values in Fig. 5b show that Radar had the highest RMSE, similar to the seasonal analysis shown in the previous section. The Gauge, TRMM-3B42RT, and TRMM-3B42V6 products had lower RMSE values than either of the PERSIANN-CCS products. The PERSIANN-CCS-MW product offered no clear improvement in terms of daily RMSE over the PERSIANN-CCS-RT product. The TRMM-3B42V6 product, on the other hand, yielded a lower RMSE than TRMM-3B42RT. Histograms of daily CORR in Fig. 5c show Gauge and then Radar had the best performance with modal values at 0.8. The next best CORR was associated with the TRMM-3B42V6 product. The real-time TRMM product performed better than both the PERSIANN-CCS products, with the PERSIANN-CCS-RT product yielding slightly higher CORR values than PERSIANN-CCS-MW.

Daily probability of detection (POD), false-alarm rate (FAR), and critical success index (CSI) contingency table statistics were computed for each of the algorithms for five exceedance thresholds. The CSI, or threat score, indicates how well the estimated rainfall amounts correspond to Stage IV rainfall above the specified thresholds.

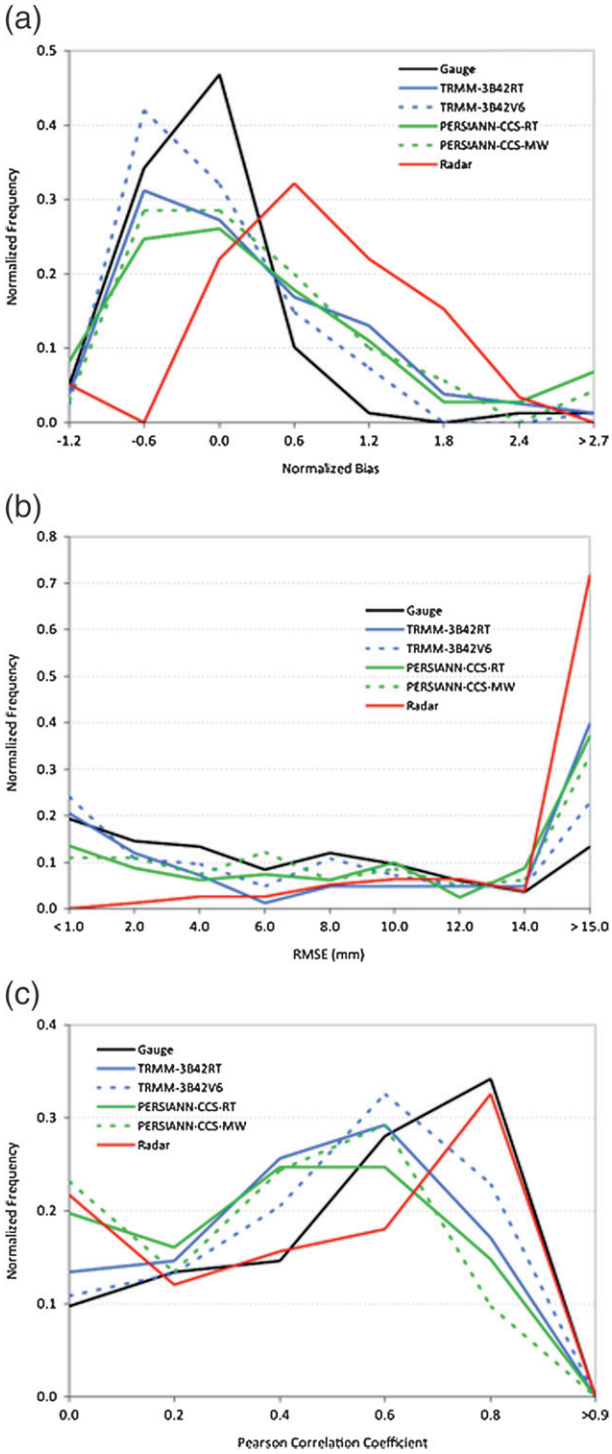

FIG. 5. Histograms of (a) NB, (b) RMSE with bias removed, and (c) Pearson correlation coefficient for daily rainfall accumulations from June to August 2007 estimated from each algorithm denoted in legend. Stage IV was considered as reference, or ground truth.

Perfect skill occurs with a CSI value of 1. The thresholds of 0.3, 1.3, 5.3, 17.4, and 51.1 mm were chosen based on the 5%, 25%, 50%, 75%, and 95% exceedance quantiles of the Stage IV daily accumulation histogram (not shown). The reader is reminded that these thresholds apply specifically to a season of record rainfall in Oklahoma and are not directly transferrable to other regions. The Gauge had the highest POD when considering 95% of the data distribution (Fig. 6a). However, Radar had the highest POD with the upper 50%, 25%, and 5% of the daily rainfall distribution. In fact, at the upper end, Gauge had the lowest detection capabilities. This is an expected result because rainfall maxima are rarely coincident with gauge locations but are captured by radar. TRMM-3B42RT had equivalent or better POD than PERSIANN-CCS-RT at all thresholds. The TRMM-3B42V6 and PERSIANN-CCS-MW performed similarly to each other and detected rainfall events better than their real-time counterparts at the lowest threshold, but less so for the upper 50%, 25%, and 5% thresholds. All algorithms tended toward lower POD values with increasing rainfall intensity.

The FAR was lowest with Gauge for all rainfall thresholds. The next lowest FAR was associated with TRMM-3B42V6. Radar had the highest FAR at the lowest threshold and then converged toward FAR values of the other satellite-based algorithms at the higher rainfall thresholds. FAR with PERSIANN-CCS-MW was higher than PERSIANN-CCS-RT for the upper 95% and 75% of the data distribution, indicating degradation in performance when microwave data were included. With the exception of Gauge, all algorithms tended toward higher FAR within increasing rainfall intensity.

The CSI, or algorithm skill, indicates the best performance was with Gauge for the upper 95%, 75%, 50%, and 25% of the Stage IV daily rainfall distribution (Fig. 6c). Interestingly, Radar was the worst performer considering 95% of the rainfall distribution, but best with high-intensity rainfall. TRMM-3B42V6 was better than or at least equivalent to TRMM-3B42RT and the two PERSIANN-CCS products for all thresholds. As noted in the daily analysis of bulk statistics, the PERSIANN-CCS-RT product outperformed PERSIANN-CCS-MW for daily rainfall accumulations. All algorithms had reduced skill with increasing rainfall intensity.

c. *Hourly composites*

Hourly rainfall composites were created by computing grids of average rainfall rate for each hour in the 3-month dataset. Figure 7a shows a time series plot of the average hourly rainfall rates, considering all grid cells in the domain (Fig. 1), for the Stage IV rainfall product. We conducted this analysis both with and without

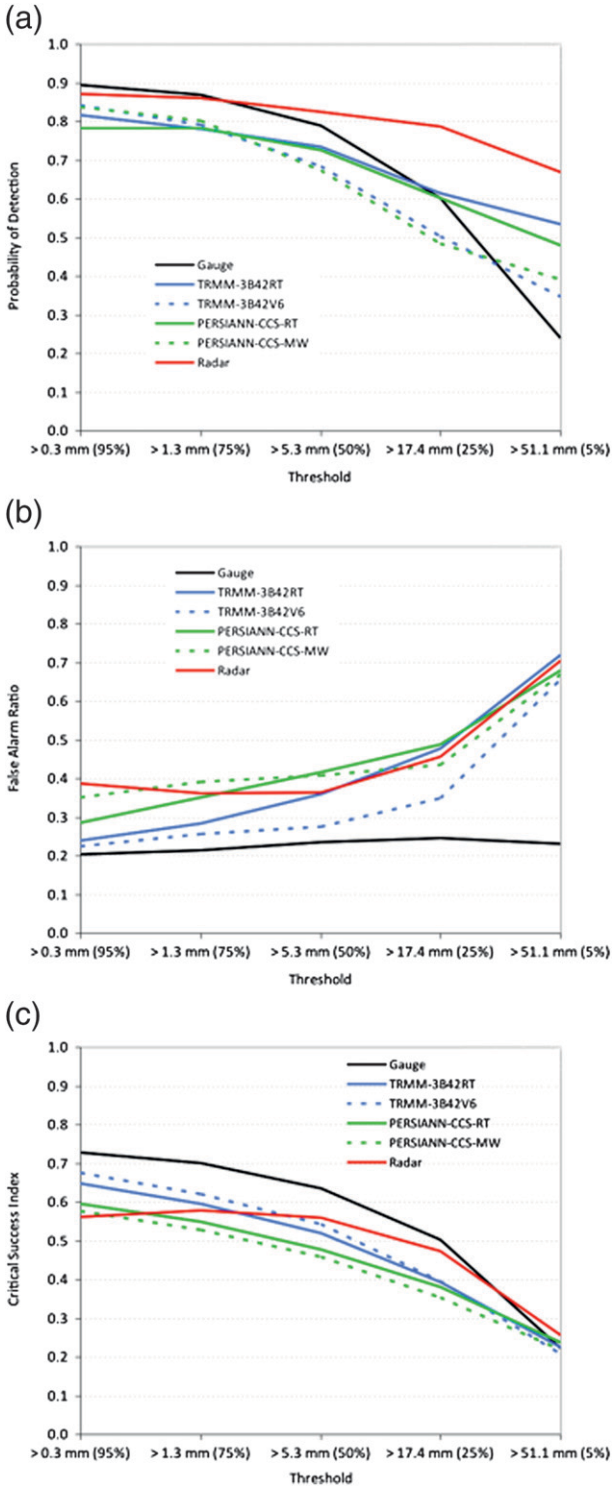

FIG. 6. Contingency table statistics for the same dataset and rainfall algorithms in Fig. 5. Threshold rainfall amounts are based on 5%, 25%, 50%, 75%, and 95% quantiles of the Stage IV daily rainfall distribution.

including data from 0900 UTC 17 August to 0900 UTC 20 August 2007, corresponding to the dates at which Tropical Storm Erin moved across the region. The intention of the hourly analysis is to determine how well each of the algorithms captures important details of the diurnal rainfall cycle. From Fig. 7a, we see rainfall reaches maximum intensity from 0900 to 1100 UTC, while there is a secondary diurnal maximum from 2100 to 2300 UTC. The discovery of the nocturnal rainfall maximum in the Great Plains dates back to the seminal work of Kincer (1916). He reported that as much as 60% of total rainfall during the warm season in the study region occurs at night; the culprit was later attributed to organized mesoscale convective complexes (Maddox 1980). The secondary rainfall maximum is caused by locally generated thunderstorms that develop with daytime peak heating. Figure 7a shows that inclusion of Tropical Storm Erin increased the average rainfall rates by approximately 0.02 mm h^{-1} for each hour of the day.

For each hourly composite, we also computed the root-mean-square deviation (RMSD) normalized by the sample mean for a 3×3 window surrounding each pixel, and reported the grid-averaged value to Fig. 7b. This metric is similar to the coefficient of variation, except the RMSD replaces the standard deviation in the numerator. In essence, this metric describes the degree of spatial variability, which we will refer to hereafter as texture, of a gridded rainfall field. Texture values have been shown to be quite useful in discriminating radar rainfall from ground clutter (Gourley et al. 2007). In Fig. 7b, inclusion of Tropical Storm Erin reduces the texture at all hours of the day, but the texture values with and without Tropical Storm Erin are approximately equal at 0900–1000 UTC, corresponding to the rainfall maximum. This means the spatial scale of Tropical Storm Erin resembles the scale of mesoscale convective complexes, which are well known to reach the southern plains during the early morning hours (Maddox 1980). The texture values can thus be interpreted as inversely proportional to the spatial scale at which storms are organized, so that high textures suggest rainfall is associated with small-scale, isolated storms. In further analyses involving hourly composites, we have subtracted out Tropical Storm Erin, because Fig. 7b indicates that including Tropical Storm Erin has the effect of reducing mean texture values associated with storm-scale, daytime convection.

By combining the results in Figs. 7a and 7b, we can envision the typical sequence of rainfall occurrence in a given day in Oklahoma during the summer of 2007. As daytime heating commences, the first thunderstorms of the day initiate around 1700 UTC and begin to produce rainfall by 1800 UTC. During the following 3–4 h,

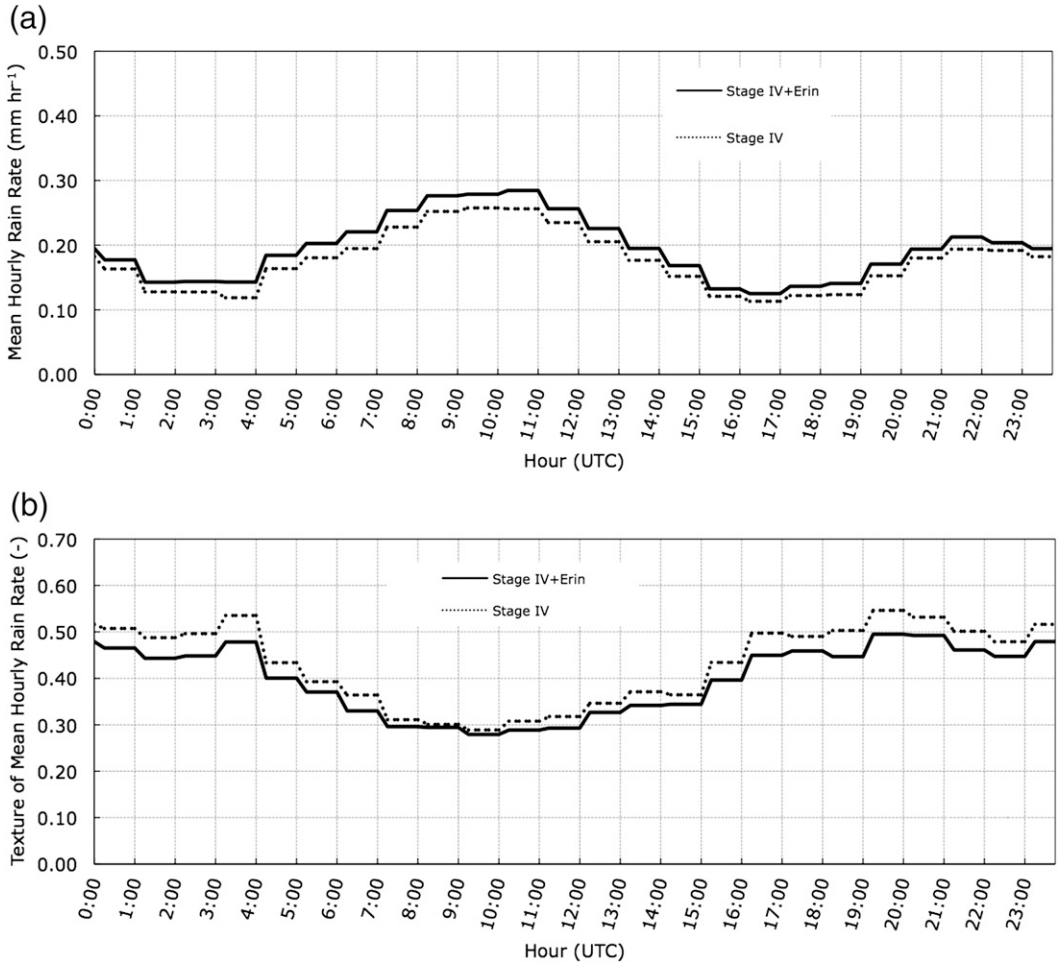

FIG. 7. Time series of grid-averaged (a) mean hourly rainfall rate from Stage IV with and without contribution of rainfall from Tropical Storm Erin and (b) texture of mean hourly rainfall rate. The texture field is defined as the RMS deviation divided by the average rainfall rate in a 3 × 3 window centered on each grid cell.

convectively driven storms become more numerous and remain isolated as noted with texture values of 0.55. A relative maximum in rainfall rates of 0.19 mm h^{-1} is reached from 2100 to 2200 UTC. At 2200 UTC, the thunderstorms begin to decay in association with loss of daytime heating. A secondary rainfall minimum of 0.12 mm h^{-1} is reached at 0400 UTC. Then, a gradual increase in grid-averaged rainfall rates occurs throughout the night reaching an overall maximum value of 0.26 mm h^{-1} from 0900 to 1100 UTC. The texture values with this nocturnal rainfall maximum are 0.3, or approximately half the values associated with the diurnal rainfall maximum. The mesoscale convective complexes impacting the region during the early morning hours are organized on a larger scale and propagate across the region as opposed to initiating within the study domain, which is the case with the diurnal rainfall maximum organized at the storm scale. Rainfall rates continue to decrease after 1100 UTC and textures increase until the minimum rainfall rate of 0.11 mm h^{-1} is reached at 1700 UTC. Hourly rainfall composites and their textures are examined for each rainfall algorithm to determine how well they describe the typical hourly sequence of rainfall occurrence during an average day in the summer of 2007.

Figure 8a shows TRMM-3B42RT having minimum rainfall rates of 0.11 mm h^{-1} at 1800 UTC in good agreement in timing and intensity with Stage IV. As rainfall rates increase with daytime heating at 2100 UTC, however, the texture of the rainfall field remains constant. The resolution of TRMM products is 3-hourly and 0.25°; the dynamic range of computed texture fields is consequentially reduced. The rainfall rates reach no secondary maximum because of isolated, convective storms but continue to increase through the nighttime hours until reaching a maximum value of 0.45 mm h^{-1} at 0600 UTC. First, the

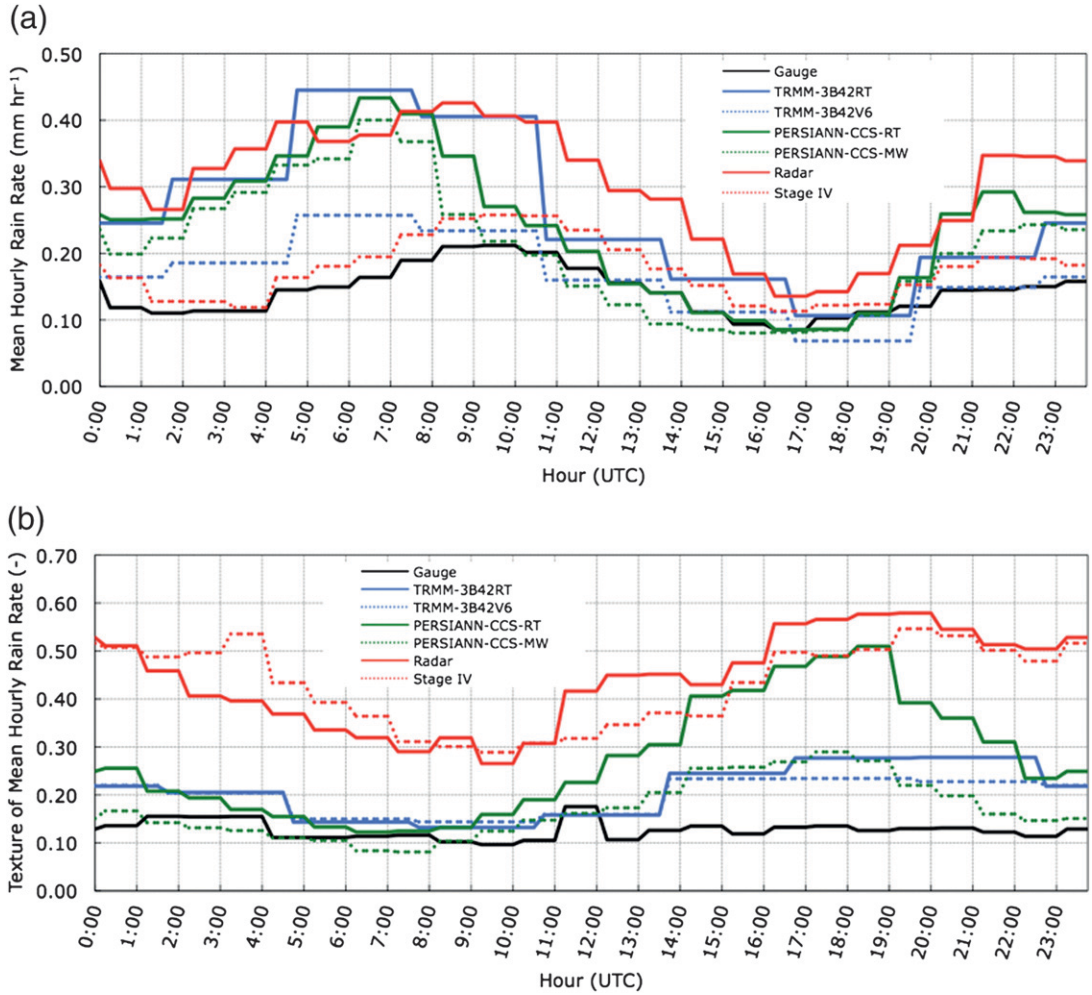

FIG. 8. As in Fig. 7, but for all rainfall algorithms examined in this study. The rainfall from Tropical Storm Erin has been omitted.

intensity of this maximum value is >70% too high. Even with the coarse, 3-hourly temporal resolution, the nocturnal rainfall maximum is reached too early. Mesoscale convective complexes are well known to be associated with large cirrus cloud shields. It is quite plausible that the cirrus cloud contamination results in the satellite-based timing error associated with the nocturnal rainfall maximum. TRMM products at 0900 or 1200 UTC are closer to the rainfall maximum as depicted by Stage IV. The TRMM-3B42RT product does, however, correctly portray a texture minimum at 0900 UTC.

The TRMM-3B42V6 product yields a very similar sequence of rainfall rates as TRMM-3B42RT, but with lower mean values reaching 0.26 mm h^{-1} at 0600 UTC. The timing of the nocturnal maximum is approximately 4 h too early, but the intensity agrees almost perfectly with Stage IV. The texture values from TRMM-3B42V6 are very similar to those of TRMM-3B42RT, but slightly lower and thus more erroneous for the daytime convection at 1800 and 2100 UTC. In general, the TRMM rainfall products depict the nocturnal rainfall maximum too early, do not indicate the secondary, diurnal maximum in rainfall rates, and do little to distinguish between the scale differences in the precipitation that produces the nocturnal and diurnal maxima. The intensity of the TRMM-3B42RT rainfall minimum, however, matches that of Stage IV, and the maximum rainfall rate of 0.26 mm h^{-1} from TRMM-3B42V6 is very close to the Stage IV maximum.

The PERSIANN-CCS-RT product in Fig. 8a has minimum rainfall rates at 1700 UTC in very good agreement with the timing of Stage IV. As daytime heating commences, rainfall rates increase to 0.29 mm h^{-1} at 2200 UTC, which overestimates the intensity of the Stage IV diurnal maximum, but the timing of the diurnal maximum is excellent. Then, rainfall rates decrease until

0200 UTC when the gradual increase with the nocturnal rainfall maximum begins. In comparison with Stage IV, the onset of this increase is approximately 2 h too early. The nocturnal maximum in rainfall rates is reached at 0700 UTC with values of 0.43 mm h^{-1}. Similar to the TRMM-3B42RT rainfall product, the timing of the maximum is approximately 3 h too early and the intensity is 65% too high. The cirrus cloud shields associated with mesocale convective systems are the likely culprit for this error affecting TRMM and PERSIANN-CCS rainfall products. The texture field with PERSICANN-CCS-RT reaches a maximum value of 0.51 at 1900 UTC in good agreement with Stage IV. Texture values decrease much more rapidly than Stage IV following the diurnal rainfall maximum and hit a minimum of 0.12 at 0700 UTC. This minimum texture value is too low and is reached about 3 h too early. Nonetheless, the PERSIANN-CCS-RT product does distinguish between the diurnal and nocturnal spatial scales of rainfall.

The PERSIANN-CCS-MW product shows the same trend in rainfall rates, but the values are approximately 0.03 mm h^{-1} lower in intensity. The lower intensities are in better agreement with Stage IV from 1900 to 0800 UTC, or just a little over half the time. In terms of depicting spatial scales of rainfall, the PERSIANN-CCS-MW product lowers the texture values at all times, which is incorrect according to Stage IV texture values. This lowering of the texture is likely due to the coarseness of the MW data (10–30 km), which was used to rescale the PERSIANN-CCS-RT product to yield PERSIANN-CCS-MW. In addition, the most correct aspect of the PERSIANN-CCS-RT texture time series, that is, the maximum of 0.51 at 1900 UTC, has been dramatically reduced to 0.29 and is now too early with its timing following inclusion of the microwave data. In summary, the PERSIANN-CCS products have similar errors as the TRMM rainfall products in that they depict the nocturnal rainfall maximum too early. They improve over TRMM in correctly resolving the secondary diurnal rainfall maximum probably due to higher temporal resolution. Moreover, the PERSIANN-CCS-RT product shows the capability of being able to differentiate the scales of precipitation that result in the nocturnal and diurnal rainfall maxima. Similar to results found with the daily statistics in section 3b, the PERSIANN-CCS-MW product offers no improvements over PERSIANN-CCS-RT.

Radar and Gauge, which the reader is reminded are both inputs to Stage IV, have very similar trends as Stage IV in Fig. 8a. There is a slight difference in the timing of the nocturnal maximum with Radar reaching values of 0.43 mm h^{-1} at 0900 UTC, 1 h prior to the Stage IV and Gauge maximum. In general, it appears as though Stage IV has been adjusted to agree more closely with the Gauge rainfall values and timing, which helps to explain the aforementioned timing difference. The time series of texture values in Fig. 8b, however, reveals Stage IV appropriately benefits from the ability of Radar to distinguish between the storm-scale diurnal maximum and the mesoscale nocturnal maximum. Future multisensor rainfall products can likewise benefit from the PERSIANN-CCS-RT product's ability to segregate the scale differences between the two rainfall maxima. The Gauge product, on the other hand, has no capability whatsoever to differentiate between these scales of organized precipitation.

4. Summary and conclusions

In this study, we have compared rainfall estimates from algorithms based on measurements from satellite, radar, rain gauges, and combinations to highlight their relative performance for seasonal, daily, and hourly time scales. This multitiered analysis considers the ability to resolve precipitation characteristics at different spatial scales and as a function of rainfall intensity. The study domain is in a heavily instrumented region in terms of radar coverage and gauge density. The topography in the study region is relatively flat and the rainfall is primarily from intense, convective storms; thus, the transferability of the results in this study may not directly apply to other regimes. Results drawn from the analysis of seasonal rainfall totals from June to August 2007 in Oklahoma are summarized as follows:

- Gauge had the highest CORR of 0.72, but underestimated rainfall by 22%.
- The Stage II radar product had the worst overall performance with overestimation of 61%, highest RMSE of 753 mm, and lowest CORR. Artifacts due to beam blockages were noted in the seasonal accumulation product.
- Despite the TRMM-3B42V6 product having relatively coarse 0.25° spatial resolution, it had the best agreement with the Stage IV product, which was considered as reference or ground truth, in terms of NB of −0.10 and RMSE of 136 mm.
- The PERSIANN-CCS-RT product had better performance than TRMM-3B42RT according to all analyzed statistics.
- The PERSIANN-CCS-MW product offered improvements over PERSIANN-CCS-RT in terms of cutting the NB and RMSE approximately in half but reduced the CORR from 0.63 to 0.60.

Rainfall rates were accumulated on a daily basis and then evaluated using histograms of NB, RMSE, and CORR bulk statistics as above, considering Stage IV as

a reference. In addition, we computed contingency table statistics for five rainfall thresholds—0.3, 1.3, 5.3, 17.4, and 51.1 mm—corresponding to the 95%, 75%, 50%, 25%, and 5% exceedance quantiles of the Stage IV daily rainfall distribution. Results from the daily rainfall analysis are summarized as follows:

- Gauge had the best performance according to the CSI for the upper 95%, 75%, 50%, and 25% of the data distribution, but worst probability of detection for the upper 5%, corresponding to extreme rainfall amounts.
- Radar, on the other hand, was the worst performer when considering rainfall accumulations >0.3 mm, but best when restricting the data sample to rainfall >51.1 mm.
- For the 95%, 75%, 50%, and 25% exceedance thresholds, TRMM products had generally higher skill than PERSIANN-CCS products, with the 3B42V6 being the best.
- Although having a lower CSI than TRMM-3B42V6 at low–medium rainfall intensity, PERSIANN-CCS-RT had the second highest skill, after Radar, at the upper 5% rainfall threshold.
- All rainfall algorithms had reduced skill with increasing rainfall rate.

The third analysis examined hourly rainfall composites from each algorithm and plotted their average rainfall rates and texture fields as a daily composite time series. The following results are summarized from the hourly analysis:

- All satellite-based products depicted the nocturnal rainfall maximum 3–4 h too early, presumably because of large cirrus shields associated with mesoscale convective complexes.
- The relatively coarse, 3-hourly resolution with the TRMM-3B42RT and TRMM-3B42V6 products inhibited their ability to properly identify the secondary, diurnal maximum in rainfall rates.
- The texture fields indicated that Gauge was unable to discriminate scale differences between nocturnal and diurnal rainfall maxima.
- PERSIANN-CCS-RT was the only satellite-based algorithm that adequately depicted the high spatial variability associated with storm-scale rainfall resulting from daytime heating.

In summary, the Stage IV product was used as a reference dataset. It was shown to be precise with the incorporation of spatial rainfall variability captured by radar while maintaining accuracy through the use of rain gauge accumulations. The ability to be simultaneously precise and accurate through the intelligent use of in situ and remote sensing platforms is a desirable characteristic of multisensor rainfall algorithms. Some potential pitfalls of the Stage IV product are quality control issues with hourly rain gauge reports and beam blockages seen in the radar data. Improvements can be expected with improved manual and automatic data quality control methods as well as using climatological radar rainfall maps to identify beam blockages and subsequently modifying hybrid scan lookup tables.

Physical limitations associated with low-Earth-orbiting satellites meant the spatiotemporal resolution of TRMM rainfall products was incapable of properly representing the diurnal cycle of rainfall in the study domain, in spite of the fact that IR data are used as input to the TRMM 3B42 algorithms (Huffman et al. 2007). The spectral analysis also revealed the lack of spatial details offered by TRMM for wavelengths up to 13 km, corresponding to approximately one-half the resolution of the 0.25° × 0.25° gridcell spacing. The result was the inability of TRMM rainfall products to distinguish between the mesoscale and storm-scale nature of nocturnal and diurnal convection. This is a major limitation if the TRMM products are to be considered for small-scale applications (e.g., flash floods and diurnal rainfall studies) in ungauged regions. The monthly gauge bias correction to the TRMM-3B42RT product to yield TRMM-3B42V6 resulted in significant improvements at all temporal scales. First, this result highlights the significance of performing bias correction, typically done with rain gauge accumulations, on remotely sensed rainfall estimates. Although recent work by Huffman et al. (2009) demonstrates how the TCI, in lieu of rain gauges, can be used to scale the TRMM-3B42RT product. Second, the gauge correction was performed on a monthly basis, yet improvements were realized submonthly at daily and hourly time scales. This result indicates the TRMM-3B42RT product has error, but the bias is stationary and thus readily correctable.

The relatively high spatiotemporal resolution with the GOES-based PERSIANN-CCS-RT product enabled it to distinguish rainfall-scale differences on an hourly basis, which justifies its use in diurnal rainfall studies in ungauged regions over TRMM rainfall products. It is noteworthy that the adjustment of PERSIANN-CCS-RT with MW data from low-Earth-orbiting satellites, yielding PERSIANN-CCS-MW, resulted in some improvements at the seasonal time scale but degraded performance at daily and hourly scales. Incorporation of MW data is meant to correct rainfall bias in a similar manner to rain gauges, but the coarseness of the MW data (10–30 km) is evidently not as sufficient as gauge data to remove bias at these smaller time scales. In addition, the update interval of recalibrating PERSIANN-CCS-RT with MW is seasonal (3-monthly), which lacks

adequate sensitivity to differences in precipitation regimes, particularly at smaller time scales such as daily or hourly. Another contributing cause might be the problematic bias of MW-based rain rates over land. Future algorithms utilizing PERSIANN-CCS rainfall products should consider using rain gauge accumulations on a monthly basis to correct bias in a similar manner to TRMM-3B42V6. The gauge-based monthly bias corrections are not available in real time; therefore, only users who are not adversely affected by the time lag (e.g., water resources) will benefit. Analyzing PERSIANN-CCS-RT with gauge bias correction at submonthly time scales (i.e., daily and/or hourly) will reveal whether the bias has a transient or stationary character. This kind of analysis will shed light on the update interval required for future recalibration strategies.

We envision that readers of this work, as well as rainfall algorithm developers, will capitalize on the benefits provided from each algorithm so they may be used in an optimal way (i.e., using a multisensor approach) to yield the most skillful rainfall products. This optimization step is particularly necessary for rainfall estimation in regions that may not have the availability of high-density instruments. For example, radar data void in the conterminous United States have been rigorously quantified in Maddox et al. (2002), while various gauge network maps show data densities and are widely available on the Internet. Future work coming from this study will be the development of a multisensor rainfall algorithm that utilizes information from radar, satellite, and gauges, and optimizes their contribution to the final product based on spatial scale, temporal scale, and rainfall intensity. Another topic inviting future research is evaluating the various rainfall algorithms as inputs to a calibrated hydrologic model at multiple temporal and spatial scales and discharge quantiles, including flash-flooding events.

Acknowledgments. Funding was provided by NOAA/Office of Oceanic and Atmospheric Research under NOAA/University of Oklahoma Cooperative Agreement NA17RJ1227, U.S. Department of Commerce. Stage II radar- and gauge-based products were provided by NCAR/EOL under sponsorship of the National Science Foundation (http://data.eol.ucar.edu/). The Stage IV rainfall product was obtained at the National Weather Service's National Precipitation Verification Unit (http://www.hpc.ncep.noaa.gov/npvu/). The authors gratefully acknowledge Dr. Soroosh Sorooshian at the University of California, Irvine, and Dr. George Huffman at NASA Goddard for providing the PERSIANN-CCS and TMPA products in this study, respectively. Reviews from Dr. George Huffman and two anonymous reviewers improved the quality of this manuscript.

REFERENCES

Anagnostou, E. N., 2004: Overview of overland satellite rainfall estimation for hydro-meteorological applications. *Surv. Geophys.,* **25,** 511–537.

Arndt, D. S., J. B. Basara, R. A. McPherson, B. G. Illston, G. D. McManus, and D. B. Demko, 2009: Observations of the overland reintensification of Tropical Storm Erin (2007). *Bull. Amer. Meteor. Soc.,* **90,** 1079–1093.

Austin, P. M., 1987: Relation between measured radar reflectivity and surface rainfall. *Mon. Wea. Rev.,* **115,** 1053–1070.

Ciach, G. J., 2003: Local random errors in tipping-bucket rain gauge measurements. *J. Atmos. Oceanic Technol.,* **20,** 752–759.

Ebert, E. E., J. E. Janowiak, and C. Kidd, 2007: Comparison of near-real-time precipitation estimates from satellite observations and numerical models. *Bull. Amer. Meteor. Soc.,* **88,** 47–64.

Gebremichael, M., and W. F. Krajewski, 2004: Characterization of the temporal sampling error in space-time-averaged rainfall estimates from satellites. *J. Geophys. Res.,* **109,** D11110, doi:10.1029/2004JD004509.

Gourley, J. J., R. A. Maddox, D. W. Burgess, and K. W. Howard, 2002: An exploratory multisensor technique for quantitative estimation of stratiform rainfall. *J. Hydrometeor.,* **3,** 166–180.

——, P. Tabary, and J. Parent-du-Chatelet, 2007: A fuzzy logic algorithm for the separation of precipitating from nonprecipitating echoes using polarimetric radar observations. *J. Atmos. Oceanic Technol.,* **24,** 1439–1451.

Hong, Y., K.-L. Hsu, S. Sorooshian, and X. Gao, 2004: Precipitation estimation from remotely sensed imagery using an artificial neural network cloud classification system. *J. Appl. Meteor.,* **43,** 1834–1853.

——, ——, ——, and ——, 2005: Self-organizing nonlinear output (SONO): A neural network suitable for cloud patch–based rainfall estimation at small scales. *Water Resour. Res.,* **41,** W03008, doi:10.1029/2004WR003142.

——, ——, H. Moradkhani, and S. Sorooshian, 2006: Uncertainty quantification of satellite rainfall estimation and Monte Carlo assessment of the error propagation into hydrologic response. *Water Resour. Res.,* **42,** W08421, doi:10.1029/2005WR004398.

——, D. Gochis, J. T. Chen, K.-L. Hsu, and S. Sorooshian, 2007: Evaluation of Precipitation Estimation from Remote Sensed Information using Artificial Neural Network-Cloud Classification System (PERSIANN-CCS) rainfall measurement using the NAME event rain gauge network. *J. Hydrometeor.,* **8,** 469–482.

Hossain, F., and G. J. Huffman, 2008: Investigating error metrics for satellite rainfall data at hydrologically relevant scales. *J. Hydrometeor.,* **9,** 563–575.

Hsu, K.-L., X. Gao, S. Sorooshian, and H. V. Gupta, 1997: Precipitation estimation from remotely sensed information using artificial neural networks. *J. Appl. Meteor.,* **36,** 1176–1190.

Huffman, G. J., and Coauthors, 2007: The TRMM multisatellite precipitation analysis (TMPA): Quasi-global, multiyear, combined-sensor precipitation estimates at fine scale. *J. Hydrometeor.,* **8,** 38–55.

——, R. F. Adler, D. T. Bolvin, and E. J. Nelkin, 2009: The TRMM Multisatellite Precipitation Analysis (TMPA). *Satellite Rainfall Applications for Surface Hydrology,* F. Hossain and M. Gebremichael, Eds., Springer Verlag, 3–22.

Joss, J., and A. Waldvogel, 1990: Precipitation measurements and hydrology. *Radar in Meteorology,* D. Atlas, Ed., Amer. Meteor. Soc., 577–606.

Joyce, R. J., J. E. Janowiak, P. A. Arkin, and P. Xie, 2004: CMORPH: A method that produces global precipitation estimates from passive microwave and infrared data at high spatial and temporal resolution. *J. Hydrometeor.,* **5,** 487–503.

Kidd, C., D. R. Kniveton, M. C. Todd, and T. J. Bellerby, 2003: Satellite rainfall estimation using combined passive microwave and infrared algorithms. *J. Hydrometeor.,* **4,** 1088–1104.

Kincer, J. B., 1916: Daytime and nighttime precipitation and their economic significance. *Mon. Wea. Rev.,* **44,** 628–633.

Legates, D. R., and T. L. DeLiberty, 1993: Precipitation measurement biases in the United States. *Water Resour. Bull.,* **29,** 855–861.

Maddox, R. A., 1980: Mesoscale convective complexes. *Bull. Amer. Meteor. Soc.,* **61,** 1374–1387.

——, J. Zhang, J. J. Gourley, and K. W. Howard, 2002: Weather radar coverage over the contiguous United States. *Wea. Forecasting,* **17,** 927–934.

Marselek, J., 1981: Calibration of the tipping-bucket raingage. *J. Hydrol.,* **53,** 343–354.

Nystuen, J. A., 1999: Relative performance of automatic rain gauges under different rainfall conditions. *J. Atmos. Oceanic Technol.,* **16,** 1025–1043.

Scofield, R. A., and R. J. Kuligowski, 2003: Status and outlook of operational satellite precipitation algorithms for extreme-precipitation events. *Wea. Forecasting,* **18,** 1037–1051.

Seo, D.-J., 1998: Real-time estimation of rainfall fields using radar rainfall and rain gage data. *J. Hydrol.,* **208,** 37–52.

Sorooshian, S., K.-L. Hsu, X. Gao, H. V. Gupta, B. Imam, and D. Braithwaite, 2000: An evaluation of PERSIANN system satellite-based estimates of tropical rainfall. *Bull. Amer. Meteor. Soc.,* **81,** 2035–2046.

Steiner, M., T. L. Bell, Y. Zhang, and E. F. Wood, 2003: Comparison of two methods for estimating the sampling-related uncertainty of satellite rainfall averages based on a large radar dataset. *J. Climate,* **16,** 3759–3778.

Turk, F. J., and S. D. Miller, 2005: Toward improving estimates of remotely-sensed precipitation with MODIS/AMSR-E blended data techniques. *IEEE Trans. Geosci. Remote Sens.,* **43,** 1059–1069.

Vasiloff, S. V., and Coauthors, 2007: Improving QPE and very short term QPF: An initiative for a community-wide integrated approach. *Bull. Amer. Meteor. Soc.,* **88,** 1899–1911.

Vicente, G. A., R. A. Scofield, and W. P. Menzel, 1998: The operational GOES infrared rainfall estimation technique. *Bull. Amer. Meteor. Soc.,* **79,** 1883–1898.

Wilson, J. W., and E. A. Brandes, 1979: Radar measurement of rainfall—A summary. *Bull. Amer. Meteor. Soc.,* **60,** 1048–1058.

Zawadzki, I. I., 1975: On radar-raingauge comparison. *J. Appl. Meteor.,* **14,** 1430–1436.